Composites: Part B 56 (2014) 536–545

Contents lists available at ScienceDirect

Composites: Part B

journal homepage: www.elsevier.com/locate/compositesb

The role of flaw size and fiber distribution on tensile ductility of PVA-ECC

Kamile Tosun-Felekoğlu [a,*], Burak Felekoğlu [a], Ravi Ranade [b], Bang Y. Lee [c], Victor C. Li [b]

[a] Department of Civil Eng., Dokuz Eylul University, İzmir, Turkey
[b] Department of Civil and Environmental Eng., University of Michigan, Ann Arbor, MI, USA
[c] School of Architecture, Chonnam National University, Republic of Korea

ARTICLE INFO

Article history:
Received 15 June 2013
Received in revised form 13 August 2013
Accepted 26 August 2013
Available online 5 September 2013

Keywords:
A. Fiber
B. Mechanical properties
D. Optical microscopy
D. Physical methods of analysis
Tensile ductility

ABSTRACT

Polyvinyl Alcohol-Engineered Cementitious Composites (PVA-ECC) designed based on micromechanics exhibit high tensile ductility (above 1%) and limited crack widths (below 100 μm). The tensile performance of ECC is dependent on the fiber and flaw size distributions. These parameters are known to be influenced by the matrix flowability and mix processing; however, a comprehensive quantitative analysis framework linking fiber and flaw size distributions to the tensile performance of PVA-ECC is needed to supplement theoretical understanding of the relationship between micromechanical parameters and composite macro-properties. In the present work, fiber distribution (dispersion and orientation) of two different ECCs in terms of matrix flowability was investigated using fluorescence microscopy and advanced digital image analysis. The maximum flaw size distribution along the specimens was also analyzed by cross-sectional image analysis. The influences of fiber and flaw size distributions on the composite behavior of PVA-ECCs were experimentally established.

1. Introduction

In recent years, Engineered Cementitious Composites (ECC) with significantly high tensile ductility and limited crack widths have emerged as a promising alternative to normal concrete and fiber reinforced concrete for improving structural performance. Micromechanically designed ECC has tensile ductility at least 100 times higher than concrete, and it utilizes moderate fiber content of 2% or less by total mix volume [1]. The design of ECC is based on micromechanics-derived scale-linking models to predict the composite behavior, which is closely dependent on the fiber and flaw size distributions along with fiber/matrix interfacial bond properties [2]. For instance, the bridging efficiency of fibers drops by up to 50%, when the fiber distribution is changed from 1D uniform alignment to 3D random distribution [3], and the ductility of ECC can be improved by more than 100% through incorporation of artificial flaws of appropriate size range [4]. The design of ECC with robust mechanical performance requires detailed knowledge of how tensile properties are governed by fiber and flaw size distributions.

Recent studies showed that the fiber and flaw size distributions in ECC are dependent on the matrix flowability and mix processing [5,6]. In a typical ECC mixing procedure, fibers are added after a plastic matrix state is achieved. An ECC matrix usually consists of cementitious materials, fine aggregate, water, and admixtures. The processing details such as mixer type, mixing speed, time and sequence, and mixing personnel's experience level can influence the homogeneity of the ECC matrix. Li and Li [5] studied the relationships between matrix rheology, fiber dispersion uniformity and composite strain capacity. The role of flaw size was not a focus on that study. Li and Wang [2] recognized the influences of both fiber dispersion uniformity and flaw size distribution on composite properties, but only quantified experimentally the flaw size distribution. A quantitative research combining the roles of fiber distribution (both dispersion and orientation) and flaw size distribution on composite tensile properties has not been reported. This paper aims to fill this knowledge gap.

The objective of this study is to systematically correlate the tensile strength and ductility of ECCs by considering the effects of three different processing parameters (largest flaw size, fiber dispersion coefficient, and fiber orientation distribution), simultaneously. It provides an effective approach to investigate the variation of ECC ductility with respect to ECC microstructure and specimen processing. For this purpose, PVA-ECC mixtures with the same mix ingredients were deliberately prepared with two different contents of HRWR admixtures. Their flowability was measured indirectly using Marsh cone flow times. The uniaxial tensile stress–strain properties were determined by using dogbone shaped specimens. After the tension tests, each dogbone specimen was sectioned at a number of locations within the gauge length. Maximum flaw size distribution, fiber dispersion coefficients, and fiber orientation distributions were measured at each cross-section. Tensile ductility differences between the specimens of each

* Corresponding author. Tel.: +90 2323017059.
E-mail address: kamile.tosun@deu.edu.tr (K. Tosun-Felekoğlu).

1359-8368/$ - see front matter © 2013 Elsevier Ltd. All rights reserved.
http://dx.doi.org/10.1016/j.compositesb.2013.08.089

ECC mixture are discussed based on this cross-sectional data analysis.

2. Research significance

To design ECC with consistent mechanical properties, it is necessary to gain a comprehensive understanding of the roles of the variability of flaw size and fiber distribution on composite tensile behavior. This paper develops quantitative linkages between the material microstructure and composite macro behavior. For this purpose different experimental techniques were applied simultaneously for the first time to determine the fiber and flaw distribution in ECC, and correlate with tensile properties. The findings of this research enhance the fundamental knowledge of the factors governing the tensile ductility of ECC. With broadening use of ECC in field applications, this fundamental knowledge becomes increasingly significant in constructing structures with reliable performance.

3. Experimental studies

3.1. Materials and mix proportions

Type I ordinary Portland cement (OPC) compliant with ASTM C150 [7] was used in all mixtures. The physical properties and chemical composition of class F fly ash used in this study are listed in Table 1. This fly ash contains significant amount of Calcium Oxide (CaO). Approximately 83% (by weight) of fly ash particles are finer than 44 μm which indicates high reactivity with the secondary hydration products. Silica sand with a maximum grain size of 250 μm and a mean size of 110 μm was utilized as fine aggregate. A polycarboxylate-based high range water reducing admixture (HRWRA) was used for the purpose of changing the matrix flowability.

PVA fibers with 39 μm diameter and 12 mm length were used. The density, nominal tensile strength, Young's modulus, elongation at rupture of PVA fibers are 1.3 g/cm^3, 1620 MPa, 42.8 GPa and 6%, respectively. In order to reduce the excessive chemical bond between fiber and matrix, the surface of the PVA fiber is oil coated (1.2% by weight) at the manufacturing stage.

ECC mixtures were prepared using a Hobart mixer with a capacity of 5 l. All solid ingredients were premixed without water for 2 min. Water and HRWRA were then added. The resulting mixture was mixed for 1 min at low speed and for 2 min at high speed, respectively. Two PVA fiber reinforced ECC mixtures were prepared with identical fiber volume fraction (2%) and matrix proportions (adopted from [8]), except that the HRWRA dosage was deliberately varied to adjust matrix flowability (see Table 2). The matrix flowability was indirectly measured using a modified Marsh cone (orifice diameter was increased to 20 mm) flow time, as described in Li and Li [5] who reported a strong linear correlation between the modified Marsh cone flow time and plastic viscosity. The flow time of ECC-I and ECC-II mixes exhibiting different flowability were 15 s and 36 s, respectively. Relatively high flow time (between 24 and 37 s) is recommended by Li [9] for achieving better PVA fiber dispersion. HRWRA induced flow difference is expected to alter the pore structure and related maximum flaw size of ECC-I and ECC-II mixes.

Table 1
Analysis results of class F fly ash from Headwaters DTE Monroe.

Chemical analysis (%)		Physical analysis	
SiO_2	44.09	Fineness (retained on 44 μm) (%)	16.85
Al_2O_3	23.21	Strength activity index 7d (%)	83
Fe_2O_3	8.39	Strength activity index 28d (%)	92
SO_3	1.46	Water requirement (% of control)	97
CaO	14.04	Autoclave soundness (%)	0
LOI	0.56	Density	2.45

3.2. Specimen preparation and mechanical tests

Fresh ECC mixtures were cast into dogbone shaped molds on a vibration table at a moderate vibration rate. The geometry of dogbone specimens conforms to JSCE [10]. Three $50 \times 50 \times 50$ mm^3 cube specimens were also prepared with the same casting procedure for compression strength tests. Specimens were demolded after 24 h. After demolding, specimens were cured in sealed plastic bags at room temperature (23 ± 3 °C) for 7 days and then stored at room temperature until the age of 28 days.

At 28 days, uniaxial tensile tests were performed with a servo-hydraulic testing frame, under displacement control (0.5 mm/min). Two external linear variable displacement transducers (LVDT) were attached to the specimen with a gauge length of 100 mm for strain measurement. The uniaxial tensile test setup is shown in Fig. 1. The uniaxial compression tests were performed in accordance with ASTM C109 [11].

3.3. Methodology of cross-section analysis

After performing the uniaxial tensile tests, the gauge length region of each dogbone specimen was sectioned into five equal pieces perpendicular to the loading direction. Ten cross-sections with surface area of 30×12.7 mm^2 were exposed in this way (Fig. 2). The saw caused a loss of approximately 3 mm of specimen thickness at each cut. Due to this reason, cross-sections facing each other exhibited different flaw and fiber distribution characteristics. For example, bottom of piece #1, section (2), is different from the top of piece #2, section (3). All cross-sections were ground with #600 and #1000 SiC paper (2 min at 200 rpm for each paper) to create a smooth surface.

3.3.1. Determination of maximum flaw size distribution

Maximum flaw size at a given cross-section determines the cracking stress of the matrix at that section in accordance with Irwin's fracture criterion. Each cross-section was photographed with a high resolution camera. Binary images were processed using thresholding in the Image-J software of the National Institute of Health (NIH), and the maximum flaw size at each cross-section was determined (Fig. 3). In some cases light colored grinding dust filled the flaws and slightly reduced the observed flaw size. Overall, the maximum flaw sizes at all cross-sections were satisfactorily determined with this technique.

3.3.2. Determination of fiber dispersion coefficient

While flaw size distributions can be determined using basic optical microscopy, more advanced techniques are needed to determine the fiber distribution, such as fluorescence microscopy combined with digital image analysis, transmission X-ray photography, and AC-impedance spectroscopy [12–16]. Fluorescence microscopy combined with digital image analysis is particularly useful for detecting Poly-vinyl Alcohol (PVA) fibers in ECC [12], and is employed in this study for quantifying fiber distribution.

Among the cross-sections obtained above for flaw size analysis, the cross-section nearest to the final failure crack was first analyzed in order to determine fiber dispersion coefficient. This cross-section is considered to be the "weakest section", where fiber bridging strength is the lowest and, therefore, determines the ultimate tensile strength of the dogbone specimen. Additionally, three more cross-sections in the vicinity of this selected section were

Table 2
The mixture proportions of PVA-ECCs with different flowability.

Mixture code	Cement (kg/m^3)	Fly ash (kg/m^3)	Silica sand (kg/m^3)	Water (kg/m^3)	PVA fiber (kg/m^3)	HRWRA (kg/m^3)
ECC-I	570	684	455	331	26	10.2
ECC-II						6.6

analyzed for comparing the fiber distribution at the "weakest section" to other cross-sections.

An Olympus BX-51 microscope suitable for bright-field and wide-field fluorescence (350–543 nm) microscopy equipped with an Olympus DP-70 high resolution digital camera was used (Fig. 4a) to capture fluorescence images of dogbone cross-sections. The specimen surface was first illuminated by a mercury lamp generating light with a broad range of wavelengths. PVA fibers are known to fluoresce and emit green light in the range of 440–460 nm when excited by ultra-violet incident light of 370–390 nm wavelength [17]. The illumination light was separated from the emitted fluorescence of considerably weaker intensity using a UV filter. Through this process, fibers under the fluorescence microscope appear as brightly colored green elliptical dots, while the surrounding cementitious matrix appears as dark gray (Fig. 4b) in cross-sectional images [12]. The fluorescence images were then captured by the DP-70 camera. For each cross-section, fifteen images (1024×1360 pixels corresponding to an area of $3.25 \times 4.30\ mm^2$) were captured from the grid-limited regions of

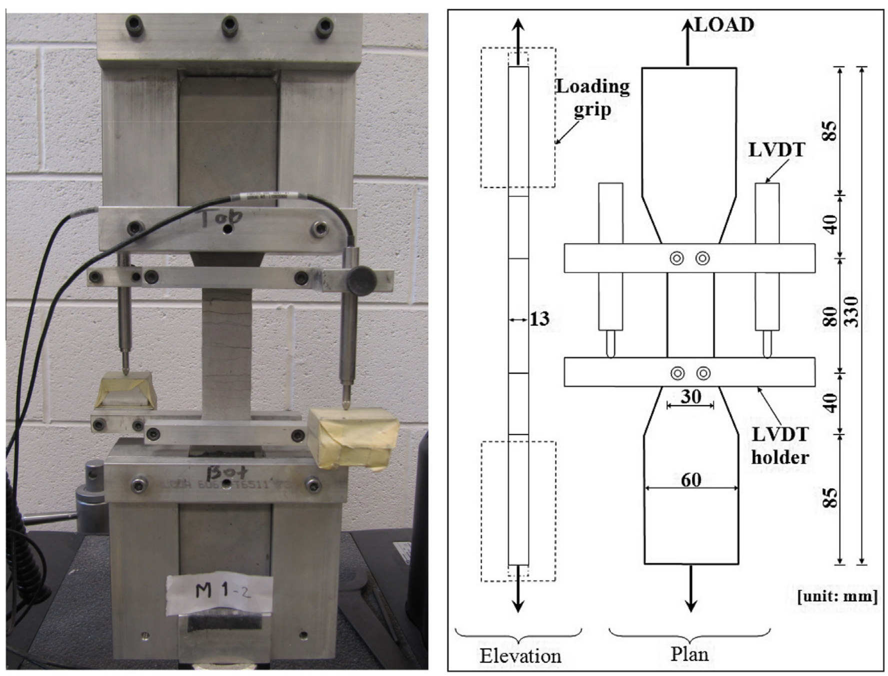

Fig. 1. Tensile test setup, specimen dimensions and LVDT configuration.

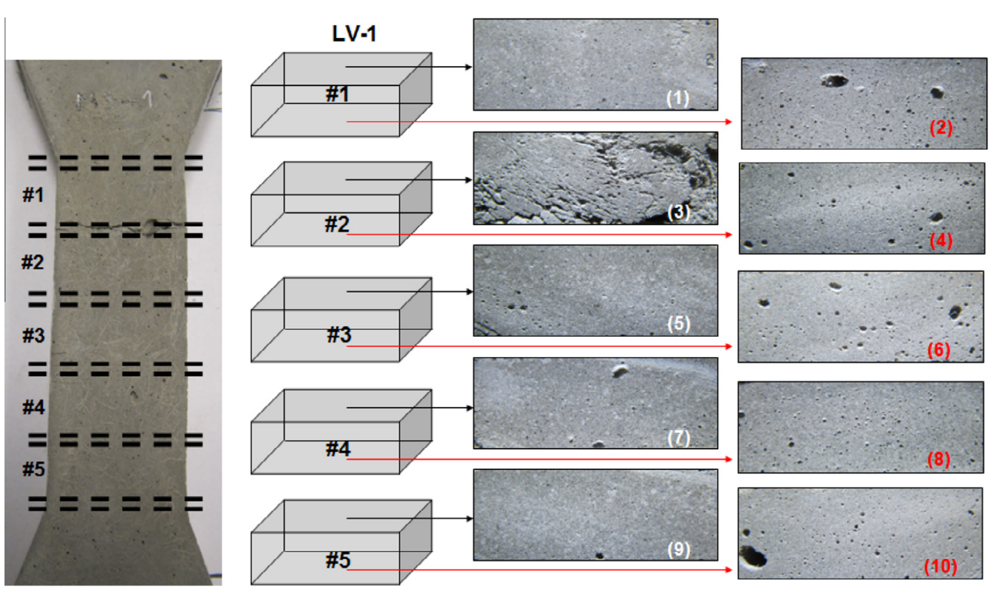

Fig. 2. Methodology of dogbone specimen cut and analyzed cross-sections.

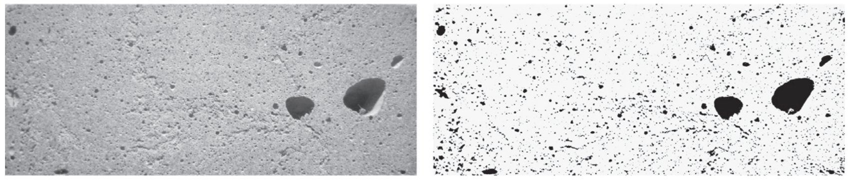
Original image (2307x975 pixel) Binary image

Fig. 3. Binarization for maximum flaw size detection by manual thresholding.

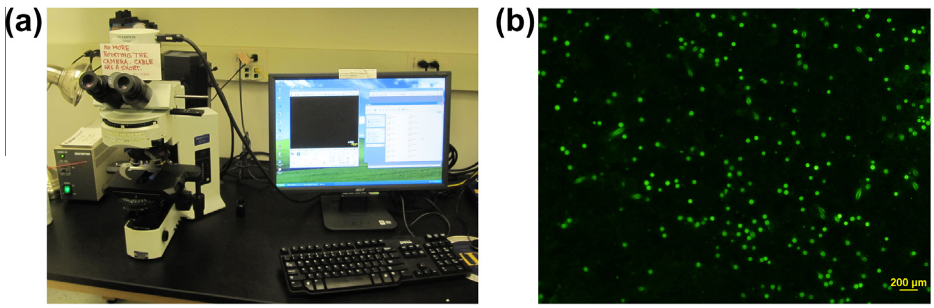

Fig. 4. (a) Olympus BX-51 Fluorescence microscope employed in this study, (b) Fluorescence image of the cutting plane, where greenish light color points represent PVA fibers.

each cross-section as illustrated in Fig. 5. In order to limit the effect of specimen edges, grid lines were started from 1 mm inside the cross-section. Scanned area with fifteen images was 70% of total effective cross-section area (($28 \times 10.7\ \mathrm{mm}^2$) of a dogbone specimen. Photographs with blurred fiber images due to inadequate polishing or presence of any major void were discarded. In this manner, good quality fluorescence images were obtained for each dogbone cross-section for fiber distribution analysis.

The fiber distribution was quantified using the deviation of the number of fibers from the average number of fibers in a unit area (cross section) [12]. The whole cross sectional image of the specimens was divided into n unit areas. The number of fibers in each unit area was counted and the coefficient of variation $\phi(x)$ was calculated (Eq. (1)). The fiber dispersion coefficient $\alpha_{Torigoe}$ was calculated as exponent of $-\phi(x)$ (Eq. (2)) [18].

$$\phi(x) = \frac{\sqrt{\frac{\sum (x_i - \bar{x})^2}{n}}}{\bar{x}} \tag{1}$$

$$\alpha_{Torigoe} = \exp[-\phi(x)] \tag{2}$$

where x_i is the number of fibers in the unit area i, $\bar{x}$ is the average number of fibers in all unit areas, and n is the number of unit areas. A dispersion coefficient of 1 indicates perfectly homogeneous fiber dispersion whereas coefficients approaching 0 indicate inhomogeneous fiber dispersion. This numerical method described in Torigoe et al. [12] was recently used by Zhou et al. [6] and Li and Li [5] in order to correlate the fiber dispersion coefficient and related tensile ductility improvement by adjusting mixing sequence and matrix viscosity, respectively.

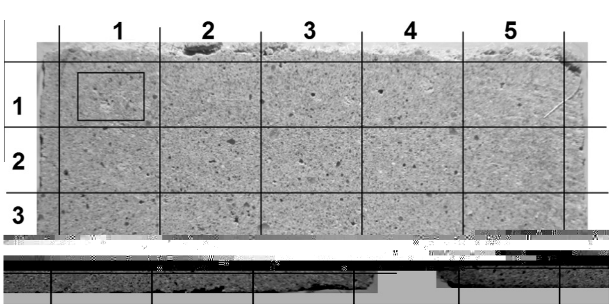

Fig. 5. Grid notation of the cutting plane and area of each captured image in comparison with whole cross-section (Small rectangle represents the area captured by microscope camera).

The fiber dispersion coefficient calculated with Torigoe's method significantly depends on the selection of the number of the unit areas (n) in which each fluorescence image is divided for the analysis. Lee et al. [19] modified this method by fixing the number of unit areas equal to the total number of fibers in an image, which effectively makes $\bar{x} = 1$ in Eq. (1). The degree of fiber dispersion is then evaluated by calculating the fiber dispersion coefficient α_{Lee}.

$$\alpha_{Lee} = \exp\left[-\sqrt{\frac{\sum (x_i - 1)^2}{n}}\right] \tag{3}$$

Lee et al. [19] also enhanced the fiber-detection performance by employing advanced digital image analysis techniques such as categorization, segmentation, watershed algorithm, and morphological reconstruction. For this purpose, a MATLAB program was developed and successfully utilized to obtain useful information about fiber distribution (dispersion and orientation) from the images captured by fluorescence microscope [17,19]. This program was used to determine the fiber dispersion coefficient (α_{Lee} in Eq. (3)) of each florescence image. Additionally, fiber dispersion coefficient values using Torigoe's approach were ($\alpha_{Torigoe}$ in Eq. (1) with $n = 15$) calculated from the variation of number of fibers at whole cross-section for comparison purpose.

3.3.3. Determination of fiber orientation distribution functions

PVA fibers with cylindrical shape project as ellipses on a cutting plane, with minor axis equal to the fiber diameter (d) and major axis (l) equal to $d/\cos\theta$, where θ is the angle with respect to loading axis (fiber inclining angle) (Fig. 6). Thus, by measuring the aspect ratio (major axis/minor axis or l/d of the ellipse), the fiber orientation can be determined by $\arccos(d/l)$. The MATLAB program developed by Lee et al. [19] is also capable of automatically calculating the inclination angle of each fiber and computing the orientation distribution data for each fluorescence image. Furthermore, it is possible to plot the best-fit probability distribution function

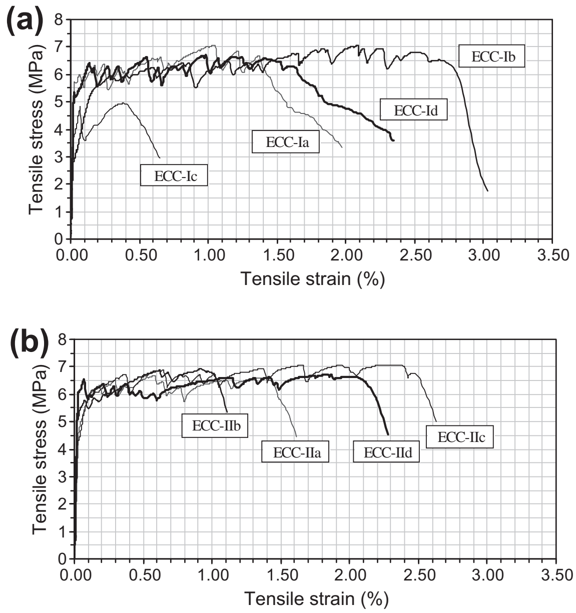

Fig. 8. Uniaxial tensile stress–strain curves of (a) ECC-I and (b) ECC-II specimens.

compared to the ECC-I specimens. For a given material processing procedure, the entrapment of air bubbles in a less flowable matrix seems more likely than a highly flowable matrix. The maximum flaw size of only 4 cross-section surface was greater than 3 mm among all ECC-I specimen cross-sections and the average of 40 sections was 2.0 ± 0.8 mm. On the other hand, maximum flaw size at 11 ECC-II specimen cross-sections was greater than 3 mm with an average maximum flaw size of 2.3 ± 1.1 mm (Fig. 9). Largest flaw size was lower than 3 mm in most of the cross-sections of both ECC-I and ECC-II specimens which seems insufficient to initiate a large number cracks required for high tensile ductility.

The percentage of cross-sections exhibiting the similar maximum flaw size in 0.5 mm intervals are plotted for ECC-I and ECC-II specimens, respectively (Fig. 10). Slight increase in the maximum flaw size in the ECC-II mix can be observed from this figure. Similar results were previously reported by Wang [21], in which the maximum flaw size range in PVA-ECC was 1.7 mm to 4.2 mm with an average of 2.8 mm. Wang [21] reported that the number of cross-sections with maximum flaw size large enough to initiate cracks was low but the tensile ductility was successfully enhanced by the addition of plastic beads into ECC mixture to act as artificial flaws.

The presence of entrapped air due to low flowability slightly lowered the 28 days compressive strength results. The average compressive strength of the ECC-II cube specimens is 70.3 ± 1.5 MPa compared to 75.2 ± 1.8 MPa of ECC-I specimens.

The first crack strength is plotted against the inverse square root of largest flaw size (largest among all maximum flaw sizes at various cross-sections) observed in various specimens in Fig. 11. A weak correlation is observed between the first crack strength and inverse square root of the largest flaw size values of both ECC-I and ECC-II specimens, which is in agreement with the fracture mechanics principles. The specimen ECC-IIb is considered an outlier in this correlation. Since a cut-plane does not usually pass through the first crack plane, the maximum flaw size on that plane may not have been captured which explain the weak correlation observed.

4.2. Fiber dispersion coefficient and orientation analysis

The fiber dispersion coefficients calculated using the approaches of Lee et al. [19] (α_{Lee} in Eq. (3)) and Torigoe et al. [12] ($\alpha_{Torigoe}$ in Eq. (1) with $n = 15$) for four cross-sections in the vicinity of the failure crack in all dogbone specimens are listed in Table 4. Out of the four cross-sections, the cross-section nearest to the failure crack is marked in bold for each dogbone specimen. While α_{Lee} is an average of 15 fiber dispersion coefficients (one for each rectangle in the grid shown in Fig. 5) computed using the approach of Lee et al. [19], $\alpha_{Torigoe}$ is a single value for the entire dogbone cross-section. As noted earlier, $\alpha_{Torigoe}$ is dependent on n. As n approaches 1 (only one image per cross-section), $\alpha_{Torigoe}$ approaches 1; and as n approaches the total number of fibers in the image, $\alpha_{Torigoe}$ approaches α_{Lee}.

Fiber dispersion coefficients calculated by using Lee et al. [19] (α_{Lee}) and Torigoe et al. [12] ($\alpha_{Torigoe}$) are plotted against tensile ductility in Fig. 12a and b, respectively. Gray and black colored symbols correspond to ECC-I and ECC-II specimen values, respectively. While the unfilled symbols in Fig. 12 represent the average fiber dispersion coefficients calculated at all four cross-sections of a dogbone specimen, the filled symbols represent the fiber dispersion coefficients at the cross-section nearest to the failure crack. Additionally, the corresponding best-fit linear correlations are also plotted in these figures (dashed and solid lines for the average of four sections and the cross-section nearest to the failure crack, respectively). Fiber dispersion coefficients calculated by using the approach of Lee et al. [19] show positive correlations with tensile ductility, i.e. better fiber dispersion leads to higher tensile ductility. The correlation is slightly stronger in the case of ECC-I specimens compared to ECC-II specimens Fig. 12a. Using the approach of Torigoe et al. [12], similar positive correlation is observed between fiber dispersion coefficients and tensile ductility in the case of ECC-I specimens. For example, lowest tensile ductility was measured from ECC-Ic specimen (0.40%) and the calculated fiber dispersion coefficients for the weakest section of this specimen were $\alpha_{Lee} = 0.220$ and $\alpha_{Torigoe} = 0.695$ (Table 4). On the other hand, ECC-Ib specimen exhibited the highest tensile ductility (2.54%) was measured from fiber dispersion coefficients for the weakest section of this specimen were $\alpha_{Lee} = 0.313$ and $\alpha_{Torigoe} = 0.808$. However, a

Table 3
Tensile properties of ECC-I and ECC-II specimens.

Mixture code	First crack strength (MPa)	Ultimate tensile strength (MPa)	Tensile ductility (%)	Number of cracks	Residual crack width (μm)
ECC-Ia	5.70	6.86	1.22	11	39
ECC-Ib	2.77	6.81	2.54	20	35
ECC-Ic	3.72	4.93	0.40	2	64
ECC-Id	5.33	6.58	1.42	21	38
ECC-I[a]	4.38 ± 1.38	6.30 ± 0.92	1.40 ± 0.88	18 ± 9	44 ± 13
ECC-IIa	4.54	6.59	1.36	13	38
ECC-IIb	5.31	6.90	0.93	9	80
ECC-IIc	4.33	7.08	2.29	18	53
ECC-IId	5.99	6.63	2.04	21	41
ECC-II[a]	5.04 ± 0.76	6.80 ± 0.23	1.66 ± 0.62	15 ± 5	53 ± 19

[a] average ± standard deviation.

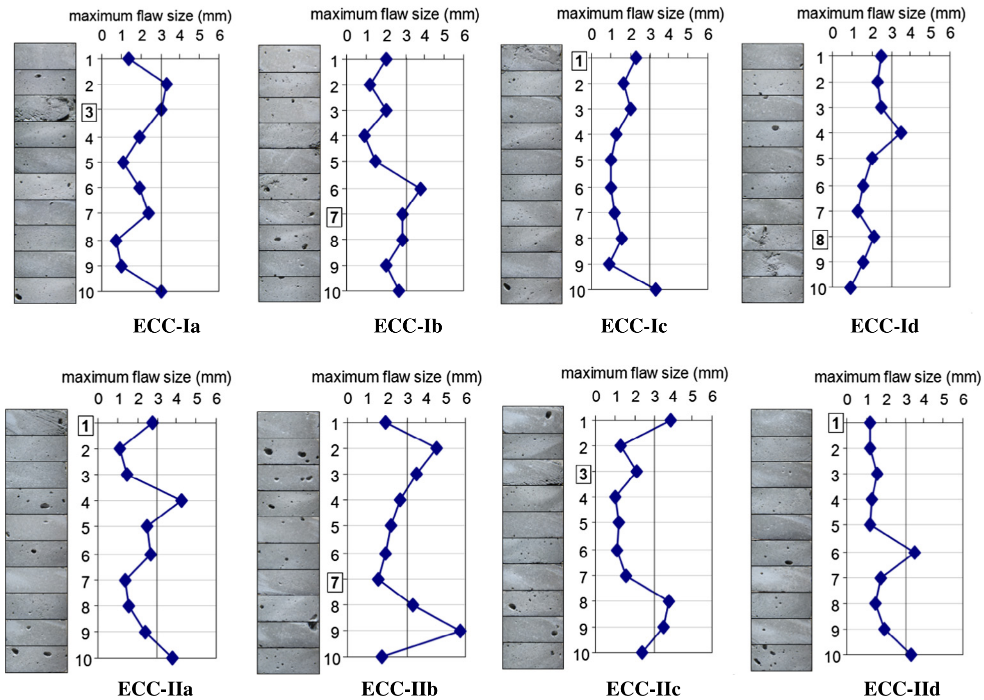

Fig. 9. Maximum flaw size distributions of ECC-I and ECC-II specimens along the loading axis.

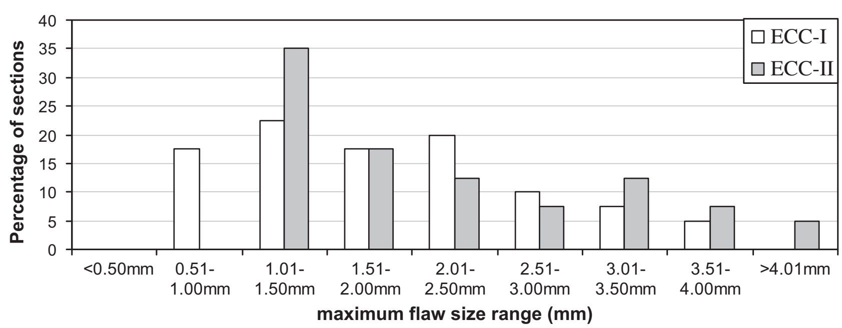

Fig. 10. Maximum flaw size distribution of ECC-I and ECC-II specimens grouped with 0.50 mm intervals.

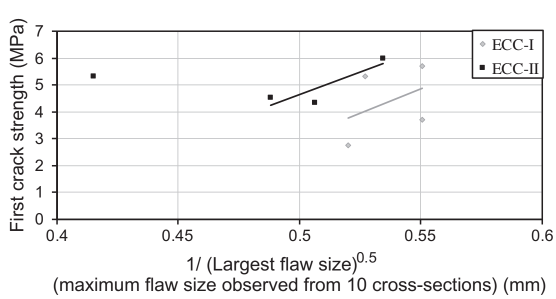

Fig. 11. Relationship between first crack strength of ECC-I and ECC-II specimens and largest flaw size values.

negative correlation is observed for ECC-II specimens in the case of Torigoe et al. [12] approach (Fig. 12b). This shows the lack of sensitivity of $\alpha_{Torigoe}$ with respect to fiber dispersion, which may be due to small value of n (15 images per cross-section) used to compute $\alpha_{Torigoe}$. α_{Lee} is a better representation of fiber dispersion compared to $\alpha_{Torigoe}$ within the results of this study.

The ultimate tensile strength values were also found to be in correlation with fiber dispersion coefficients (α_{Lee}), i.e. better fiber dispersion leads to higher ultimate tensile strength. As plotted in Fig 13, this correlation was more significant in the case of ECC-I series. In general, the ultimate tensile strength of materials is associated with largest flaw size since the largest flaw is supposed to create the weakest section. However, in the case of ECC, the ultimate tensile strength is governed by the minimum capacity of bridging fibers among all cracked planes in the process of multiple cracking. The largest flaw along the whole length only controlled the first crack strength and not the ultimate strength. As seen from the results of ECC-I and ECC-II specimens there is no correlation with the ultimate strength and largest flaw size (Table 3, Fig. 9). While ECC-Ic specimen with low α_{Lee} value (0.220) exhibited lowest ultimate tensile strength (4.93 MPa) among other specimens, largest flaw size of this specimen was only 3.2 mm. On the other hand, ECC-Ic specimen with high α_{Lee} (0.313) exhibited higher ultimate tensile strength (6.81 MPa) with a higher largest flaw size (3.8 mm). These results confirmed that the final failure and related ultimate tensile strength of ECC are governed by the fiber dispersion (which in turn governs the fiber bridging capacity) rather than largest flaw size.

Best-fit fiber orientation distributions instead of theoretically expected 2D uniform distribution) are determined using 60 fluo-

Table 4
Fiber dispersion coefficients calculated by Lee et al. [19] and Torigoe et al. [12] approach.

Cross-section (vertical order)	α_{Lee}	$\alpha_{Torigoe}$	Cross-section (vertical order)	α_{Lee}	$\alpha_{Torigoe}$
ECC-Ia (3)[a]	**0.315**	**0.741**	**ECC-IIa (1)**[a]	**0.293**	**0.913**
ECC-Ia (4)	0.296	0.805	ECC-IIa (2)	0.299	0.860
ECC-Ia (5)	0.293	0.820	ECC-IIa (3)	0.294	0.879
ECC-Ia (6)	0.293	0.858	ECC-IIa (4)	0.301	0.850
ECC-Ib (5)	0.339	0.828	ECC-IIb (7)[a]	0.307	0.848
ECC-Ib (6)	0.307	0.806	ECC-IIb (8)	0.291	0.845
ECC-Ib (7)[a]	**0.313**	**0.808**	**ECC-IIb (9)**	**0.311**	**0.839**
ECC-Ib (8)	0.299	0.835	ECC-IIb (10)	0.310	0.848
ECC-Ic (1)[a]	**0.220**	**0.695**	**ECC-IIc (1)**	**0.323**	**0.763**
ECC-Ic (2)	0.275	0.791	ECC-IIc (2)	0.325	0.847
ECC-Ic (3)	0.244	0.781	ECC-IIc (3)[a]	0.313	0.863
ECC-Ic (4)	0.297	0.836	ECC-IIc (4)	0.314	0.811
ECC-Id (7)	0.284	0.815	ECC-IId (1)[a]	0.315	0.854
ECC-Id (8)[a]	**0.308**	**0.795**	**ECC-IId (2)**	**0.333**	**0.811**
ECC-Id (9)	0.298	0.811	ECC-IId (3)	0.320	0.800
ECC-Id (10)	0.311	0.854	ECC-IId (4)	0.329	0.841

α_{Lee} : Average of 15 values at each cross section image, $\alpha_{Torigoe}$: Single value.
[a] Cross-section nearest to failure crack (refer to Fig. 2 for vertical cross-section numbers in parentheses).

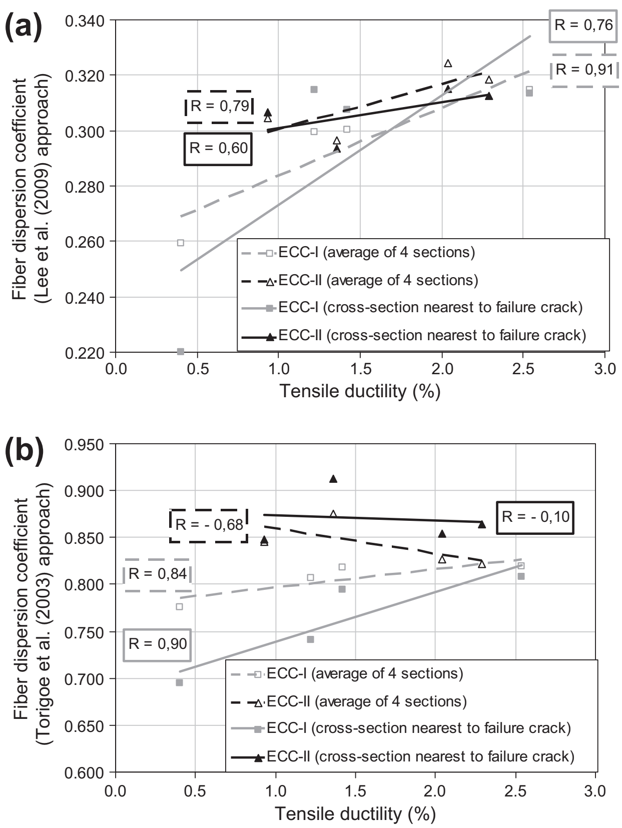

Fig. 12. Fiber dispersion coefficients calculated by (a) Lee et al. [19] approach and (b) Torigoe et al. [12] approach, and related tensile ductility values.

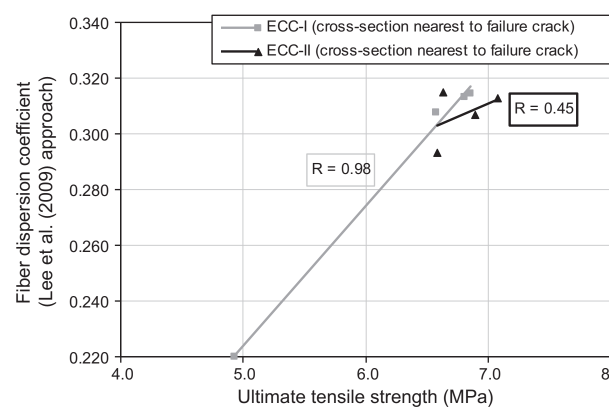

Fig. 13. The relationship between ultimate tensile strength and fiber dispersion coefficients (α_{Lee}).

rescence images (4 cross-sections times 15 images per cross-section) captured for each dogbone specimen. Only the peak point of each probability distribution function, representing the mode of the distribution, is plotted in Fig. 14 for ECC-I (left column) and ECC-II (right column) specimens – each graph in Fig. 14 represents one dogbone specimen. The filled symbols correspond to the cross-section nearest to final failure crack (shown in bold in the legend of the Fig. 14). The modes of the distributions shown in Fig. 7a–c are also pointed out in Fig. 14.

Fig. 14 provides significant insights into the orientation distribution of fibers in various dogbone specimens tested in this study. The highest density of points is between the smaller inclination angles of 15° and 45° with respect to the longitudinal (or loading) axis of the dogbone specimens. Additionally, the magnitude of these modes (ordinate $p(\theta)$) increases at smaller inclination angles. Both these observations may be caused by the casting process in which the fresh plastic material flows along the longitudinal axis of the specimen. Limited freedom of rotation of fibers in the third dimension (specimen thickness) is another factor that increases the number of fibers oriented at smaller angles [17]. Thus, the fiber orientations are influenced by the specimen geometry, as expected.

In addition to the real effect of the specimen geometry on fiber orientation, limitations of the fiber orientation detection and imaging procedure may also influence the orientation distribution. For instance, the aspect ratio (function of $\cos\theta$) of the fiber image, which is used to determine fiber orientation, changes by only about 6% between 0° and 20° which is sometimes higher than the stigmatism error in the microscope images causing all fibers in 0–20° range to be counted with angles equal to or greater than 20°. Similarly, highly inclined fibers (between 80° and 90°) tend to bend due to their low transverse stiffness, which reduces the aspect ratio of their projection on the section plane and are, therefore, detected as less inclined fibers [17]. Despite these limitations, fiber orientation distributions provide valuable data to interpret the relative variability in tensile ductility of dogbone specimens tested in this study.

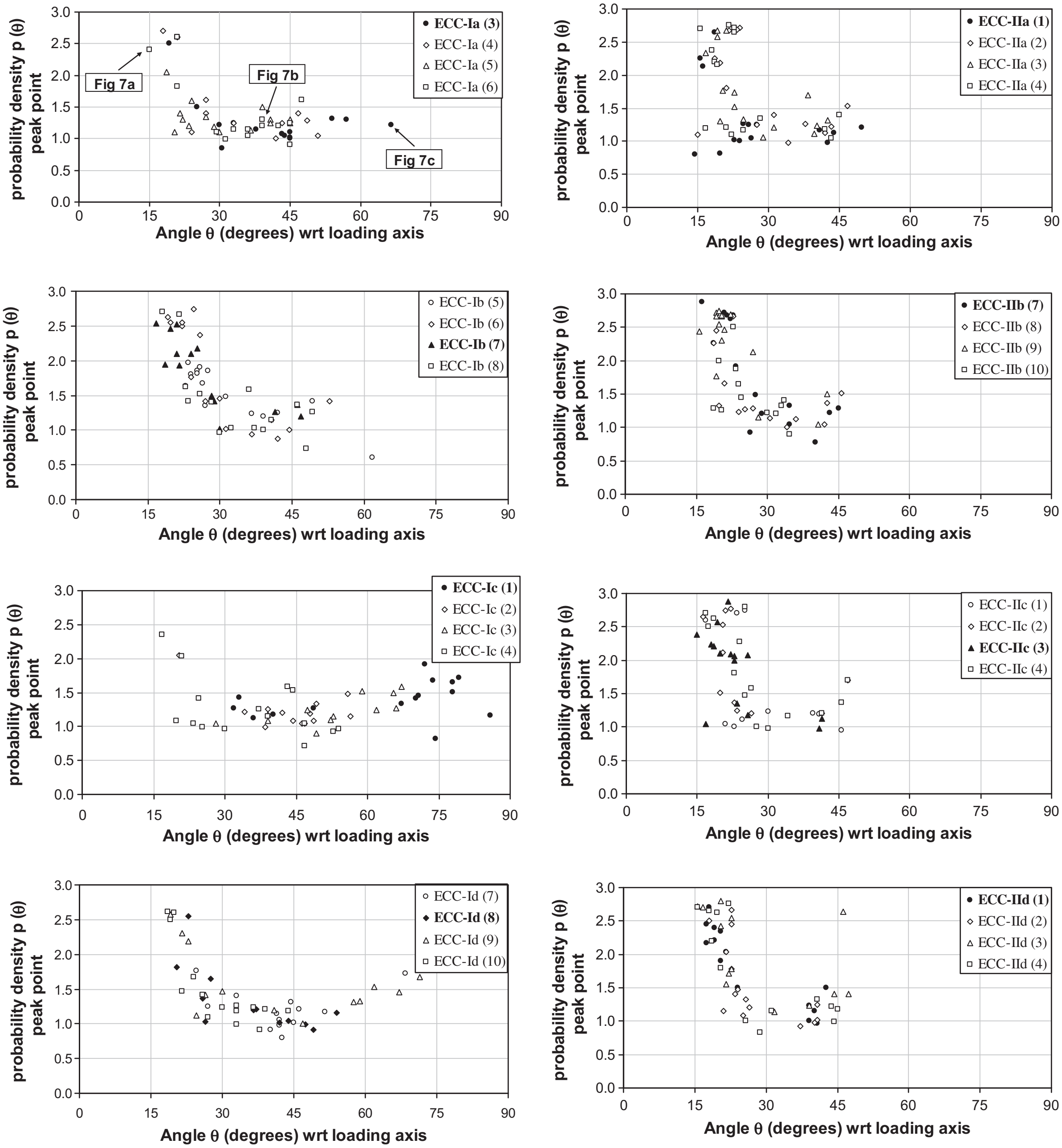

Fig. 14. Modes (peak points) of orientation distributions between 0° and 90° w.r.t. loading axis. Left column: ECC-I specimens; Right column: ECC-II specimens.

The influence of fiber orientation distributions on the tensile ductility of ECC-I specimens can be investigated by using Table 3 and Fig. 14. Among all ECC-I specimens, ECC-Ib exhibited the highest tensile ductility of 2.54%. From Fig. 14, it can be observed that majority of fibers at all cross-sections are oriented between 15° and 50°. These highly oriented fibers along loading axis significantly improved the tensile ductility of this specimen. In contrast, ECC-Ic shows the widest scatter of the modes of fiber orientation distributions. Furthermore, most of the fibers at the failure section are oriented above 65°, which significantly reduces the fiber bridging efficiency. As a result, the tensile ductility of this specimen was only 0.40%. The modes of fiber orientation distributions of ECC-Ia and ECC-Id are similarly spread between 15° and 75° at all cross-sections. Tensile ductility of these specimens was limited to 1.22% and 1.42%, respectively. In general, the ECC-I specimens with more number of fibers aligned with the loading axis (smaller inclination angles) show higher tensile ductility than the specimens with less aligned fibers.

Compared to ECC-I specimens, ECC-II specimens showed narrower scatter in the modes of the fiber orientation distributions, which ranged from 15° to 45°. Such narrower scatter in fiber orientation distribution led to more consistent tensile ductility values in the range of 0.93–2.29% in ECC-II specimens compared to 0.40–2.54% in ECC-I specimens. It can be concluded that cohesive matrix in ECC-II specimens due to comparatively low flowability is beneficial for achieving consistent fiber orientation distribution and, therefore, result in more consistent mechanical properties.

5. Conclusions

This study establishes the framework for studying the influence of fiber and flaw size distributions on the tensile strength and ductility of ECCs exhibiting different microstructures. Based on the results, the following conclusions can be drawn:

1. Tensile ductility and ultimate tensile strength of ECCs can be characterized by the fiber dispersion coefficients α_{Lee}. High α_{Lee} is beneficial to the tensile performance of ECC.
2. A correlation is observed between the first crack strength and inverse square root of the largest flaw size values of ECC specimens while no correlation was observed between the ultimate tensile strength and the largest flaw size.
3. A more cohesive matrix (as that for ECC-II) is beneficial for achieving more consistent mechanical properties due to a narrower scatter in fiber orientation distribution. In contrast, a wide scatter in the modes of fiber orientation distributions at various cross-sections of a specimen resulted in more variable tensile ductility (ECC-I). Highly inclined fibers reduces the fiber bridging efficiency, and therefore, tensile ductility of ECC specimens.
4. Two techniques of computing fiber dispersion coefficients were compared in this study in terms of their correlation with tensile ductility. Of the two techniques, fiber dispersion coefficient α_{Lee} is found to be a better representation of fiber dispersion compared to $\alpha_{Torigoe}$. The lack of sensitivity of $\alpha_{Torigoe}$ with respect to fiber dispersion is due to small value of n (15 images per cross-section) used to compute this coefficient.

Acknowledgements

This study was conducted at Advanced Civil Engineering – Materials Research Laboratory (ACE-MRL: http://ace-mrl.engin.umich.edu/), University of Michigan, Ann Arbor, MI. Financial support for the first author provided by YOK (The Council of Higher Education, Turkey) is acknowledged. The second author is grateful to TUBITAK (The Scientific and Technological Research Council of Turkey) under the Grant no. 2219 (International post-doctoral research fellowship programme) for the fellowship, which made it possible to conduct this research at the University of Michigan. Materials supply from Lafarge (cement), Headwaters (fly ash), WR Grace (HRWRA), and Kuraray (PVA fiber) is also gratefully acknowledged.

References

[1] Li VC. From micromechanics to structural engineering – the design of cementitious composites for civil engineering applications. JSCE J Struct Mech Earthquake Eng 1993;10(2):37–48.
[2] Li VC, Wang S. Microstructure variability and macroscopic composite properties of high performance fiber reinforced cementitious composites. J Probabilistic Eng Mechs 2006;21(3):201–6.
[3] Li VC, Wang Y, Backer S. A micromechanical model of tension softening and bridging toughening of short random fiber reinforced brittle matrix composites. J Mech Phys Solids 1991;39(5):607–25.
[4] Wang S, Li VC. Tailoring of pre-existing flaws in ECC matrix for saturated strain hardening. In: Proceedings of FRAMCOS-S; 2004. p. 1005–12.
[5] Li M, Li VC. Rheology, fiber dispersion, and robust properties of Engineered Cementitious Composites. Mater Struct 2013;46(3):405–20.
[6] Zhou J, Qian S, Ye G, Copuroglu O, van Breugel K, Li VC. Improved fiber distribution and mechanical properties of engineered cementitious composites by adjusting the mixing sequence. Cem Concr Compos 2012;34(3):342–8.
[7] ASTM C150). Standard Specification for Portland Cement, Annual Book of ASTM Standards, PA, USA; 2012.
[8] Yang E-H. Designing added functions in engineered cementitious composites. The University of Michigan, Ph.D. Thesis (Civil Engineering); 2007. 276p.
[9] Li M. Multi-scale design for durable repair of concrete structures. The University of Michigan, Ph.D. Thesis (Civil Engineering); 2009. 425p.
[10] JSCE. Recommendations for design and construction of high performance fiber reinforced cement composites with multiple fine cracks. Tokyo: Japan Soc. of Civil Engineers; 2008.
[11] ASTM C109. Standard Test Method for Compressive Strength of Hydraulic Cement Mortars (Using 2-in. or [50-mm] Cube Specimens). Annual Book of ASTM Standards, PA, USA; 2012.
[12] Torigoe S, Horikoshi T, Ogawa A, Saito T, Hamada T. Study on evaluation method for PVA fiber distribution in engineered cementitious composite. J Adv Concr Technol 2003;1(3):265–8.
[13] Guild FJ, Summerscales J. Microstructural image analysis applied to fibre composites materials: a review. Composites 1993;24(5):383–93.
[14] Akkaya Y, Shah SP, Ankenman B. Effect of fiber dispersion on multiple cracking of cement composites. J Eng Mater Civil Eng 2001;127(4):311–6.
[15] Yang Y. Methods study on dispersion of fibers in CFRC. Cem Concr Res 2002;32(5):747–50.
[16] Ozyurt N, Mason TO, Shah SP. Correlation of fiber dispersion, rheology and mechanical performance of FRCs. Cem Concr Compos 2007;29(2):70–9.
[17] Ranade R, Stults MD, Lee B, Li VC. Effects of fiber dispersion and flaw size distribution on the composite properties of PVA-ECC. In: Parra-Montesinos GJ, Reinhardt HW, Naaman AE. In: Proc., Sixth Int'l Workshop on High Performance Fiber Reinforced Cement Composites (HPFRCC6), Ann Arbor, MI; 2011. p. 106–13.
[18] Kobayashi K. Fiber reinforced concrete. Tokyo: Ohm-Sha; 1981.
[19] Lee BY, Kim JK, Kim JS, Kim YY. Quantitative evaluation technique of Polyvinyl Alcohol (PVA) fiber dispersion in engineered cementitious composites. Cem Concr Compos 2009;31(6):408–17.
[20] Xia M, Hamada H, Maekawa Z. Flexural stiffness of injection molded glass fibre reinforced thermoplastics. Int Polym Process 1995;10(1):74–81.
[21] Wang, S. Micromechanics Based Matrix Design for ECCs. The University of Michigan, Ph.D. Thesis (Civil Engineering); 2005. 222p.